Microtube Surfaces for Simultaneous Enhancement of Efficiency and Critical Heat Flux during Pool Boiling

*Youngsup Song[1], Shuai Gong[2], Geoffrey Vaartstra[1], Evelyn N. Wang[1],**

[1]Department of Mechanical Engineering, Massachusetts Institute of Technology, Cambridge, MA 02139, USA

[2]School of Mechanical Engineering, Shanghai Jiao Tong University, Shanghai 200240, China

KEYWORDS

Boiling, Critical heat flux, Heat transfer coefficient, Phase change heat transfer, Microsurfaces

ABSTRACT

Boiling is an essential process in numerous applications including power plants, thermal management, water purification, and steam generation. Previous studies have shown that surfaces with microcavities or biphilic wettability can enhance the efficiency of boiling heat transfer, i.e., the heat transfer coefficient (HTC). Surfaces with permeable structures such as micropillar arrays, in contrast, have shown significant enhancement of the critical heat flux (CHF). In this work, we

investigated microtube structures, where a cavity is defined at the center of a pillar, as a structural building block to enhance HTC and CHF simultaneously in a controllable manner. We demonstrated simultaneous CHF and HTC enhancements of up to 62% and 244%, respectively, compared to those of a smooth surface. The experimental data along with high-speed images elucidate the mechanism for simultaneous enhancement where bubble nucleation occurs in the microtube cavities for increased HTC and microlayer evaporation occurs around microtube sidewalls for increased CHF. Furthermore, we combined micropillars and microtubes to create surfaces that further increased CHF by achieving a path to separate nucleating bubbles and rewetting liquids. This work provides guidelines for the systematic surface design for boiling heat transfer enhancement and has important implications for understanding boiling heat transfer mechanisms.

INTRODUCTION

Boiling plays an essential role in numerous applications such as steam power plants, thermal management, and water treatment.[1] In fact, roughly 88% of energy and 80% of electricity in the United States in 2019 were produced by steam turbines with conventional and renewable resources such as natural gas, coal, nuclear energy, biomass, and geothermal energy, where the steam is generated through a boiling process.[2] In addition to energy production, steam generation is widely employed in industrial food and chemical processing, water purification, and sterilization.[3-6] Furthermore, boiling has potential in the thermal management of high-power-density systems such as concentrated photovoltaics and integrated electronics by harnessing the large latent heat of vaporization.[7-8] Increasing demand and complexity of boiling applications

implies the greater importance of achieving enhanced boiling performance through surface design and engineering.

Pool boiling performance is characterized mainly by two parameters: the heat transfer coefficient (HTC, h) and critical heat flux (CHF, $q"_{\mathrm{CHF}}$). The HTC (h) in saturated boiling is defined as the ratio of the heat flux (q'') to the temperature difference between the boiling surface (T_{w}) and the saturated bulk fluid (T_{sat}), i.e., $h = q"/\Delta T_{\mathrm{w}}$, where $\Delta T_{\mathrm{w}} = T_{\mathrm{w}} - T_{\mathrm{sat}}$ is the wall superheat. A higher HTC requires a lower superheat to attain a specified heat flux, which improves the efficiency of the boiling heat transfer. The CHF ($q"_{\mathrm{CHF}}$), on the other hand, represents the operational limit of nucleate boiling. When an applied heat flux exceeds the CHF, the transition happens from nucleate boiling to film boiling, where vapor films formed over the surface abruptly increase thermal resistance. This transition above the CHF point, known as the boiling crisis or departure from nucleate boiling, leads to a drastic increase in wall superheat, which results in catastrophic device burnout and system failure.[9]

Previous studies have shown that engineered surfaces can significantly enhance the boiling performance. Surfaces with microcavities or heterogeneous wettability patterns, for example, have improved HTC values by promoting vapor bubble nucleation (Figure 1a).[10-13] Surfaces with permeable structures such as micropillars, in contrast, have shown significant enhancement of CHF values by harnessing contact line augmentation and capillary-fed rewetting, i.e., surface wickability (Figure 1b).[14-19] In particular, a strong relationship between CHF values and the surface wickability has been widely reported.[16-17, 20] A few studies have combined micro-permeable structures (micropillars or microchannels) with functional coatings, e.g., self-assembled monolayers, reduced graphene oxide membranes, and porous copper layers, which exploit micro-permeable structures and the coatings to enhance CHF and HTC values,

respectively.[21-24] The addition of nanostructures to microstructures or to heterogeneous wettability patterns have shown further increases in CHF and HTC values;[11, 16-17, 25-26] however, these approaches are less durable than microstructures and have limited control over boiling performance, due to the random nature of nanostructures and limited variability of heterogeneous wettability materials.[27-28]

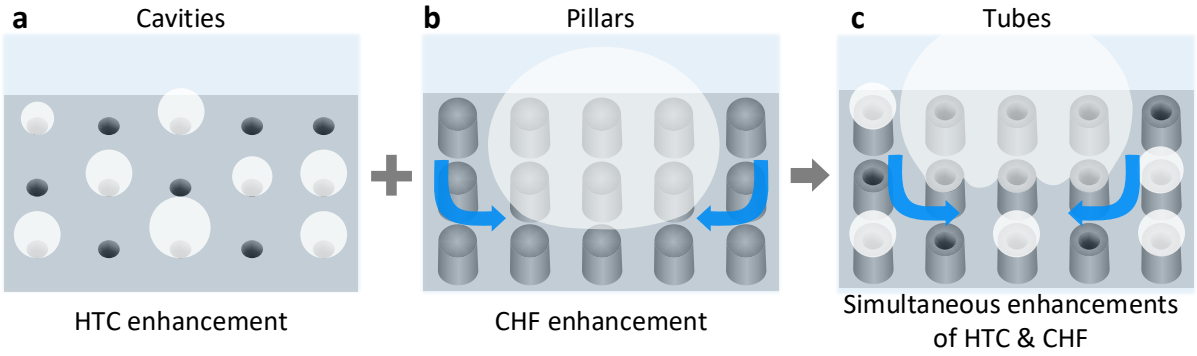

Figure 1. Microsurfaces and their effects on pool boiling heat transfer enhancement. (a) Cavities promote vapor bubble nucleation and enhance HTC values. (b) Pillar arrays provide enhanced CHF values by contact line augmentation and capillary-fed rewetting. (c) Tube arrays, where a cavity is defined at the center of a pillar, enable simultaneous enhancement of both HTC and CHF values.

In this work, we designed and investigated precisely controlled microtube structures (Figure 1c), where a cavity is defined at the center of a pillar, as a microscale structural building block to enhance HTC and CHF values simultaneously. Cavities are designed to induce vapor trapping and bubble nucleation for HTC enhancement, while the sidewalls of the microtube arrays provide CHF enhancement as micropillar arrays. Moreover, the designed microtube arrays enable effective separation of vapor and liquid paths during the bubble generation and departure

cycles, where bubbles nucleate at the top of the microtubes while liquid rewets the surface through the microtube sidewalls. The separation of vapor and liquid paths was demonstrated to be effective for boiling enhancement on copper surfaces with modulated porous-layer coatings of spherical copper particles and contoured microchannels.[29-30] In addition to uniform microtube arrays, we designed surfaces with microtube clusters interspersed with micropillars, referred to as TIP (tube-clusters in pillars), to reduce the coalescence of bubbles from the micro-tubes. While microtube arrays may enhance HTC and CHF values compared to a smooth surface, we postulated that uniform microtube arrays might not achieve as high CHF values as micropillar arrays due to the drastically higher nucleation site density. Previous studies have suggested that the boiling crisis may be a result of the stochastic interaction of bubbles; in other words, an excessive nucleation site density, i.e., cavity density, may lead to an earlier boiling crisis.[31-34]

EXPERIMENTAL

To investigate the effects of microtube surface structures on pool boiling heat transfer compared to other structures, we fabricated micropillar, microcavity, microtube arrays, and TIP surfaces by photolithography and deep reactive-ion etching processes on silicon wafers (Figure 2). The surfaces were coated with a 100-nm-thick SiO_2 layer at the end of the fabrication process by plasma-enhanced chemical vapor deposition to ensure uniform hydrophilicity over the entire surface. The details of the fabrication process are supplied in Section I of the Supporting Information. The outer diameter (d), height (h), and pitch (p) of micropillar (Figure 2a) and microtube (Figure 2d, e) arrays were 22, 30, and 40 μm, respectively. The depth of the microcavity arrays was ~30 μm (Figure 2b). The cavity diameter (d_c) of microcavity and

microtube arrays is directly related to the excess pressure in a bubble embryo ($\Delta P = \sigma/d_c$, where σ is liquid-vapor surface tension) required to initiate nucleate boiling. Combined with the Clausius-Clapeyron relation, the excess pressure can be expressed as the wall superheat for the onset of nucleate boiling, i.e., $\Delta T_{ONB} \approx \frac{2\sigma T_{sat}}{h_{fg}\rho_g(d_c/2)}$, where h_{fg} and ρ_g are latent heat of vaporization and vapor density, respectively.[35] The inverse relation between ΔT_{ONB} and d_c plotted in Figure 2c shows that bubbles can more readily nucleate on a larger cavity as long as the cavity radius is much smaller than the thermal boundary layer thickness δ_t, e.g., $\delta_t \sim \mathcal{O}$(-4) m for saturated water at atmospheric pressure, which is an order of magnitude larger than d_c ($\mathcal{O}$(-6) - $\mathcal{O}$(-5) m).[36] We fabricated microcavity and microtube arrays with d_c of 5 μm and 12 μm, which correspond to ΔT_{ONB} of 11℃ and 5℃, respectively, to investigate the effects of cavity size. A TIP surface with microtube clusters (300 × 300 μm^2) that were 2 mm apart from each other with micropillars between clusters is shown in Figure 2f, where the cluster-to-cluster pitch of 2 mm is based on the capillary length of water $l_c = \sqrt{\sigma/(\Delta\rho g)} \approx 2.5$ mm which was found to be efficient to separate nucleating bubbles.[37] We named each surface according to its structure and cavity size as shown in Figure 2.

The pool boiling rig consists of a glass chamber fixed at both ends by polyetherimide blocks, and the 20 × 20 mm^2 test sample attaches at the bottom of the chamber with adhesive sealant. On the backside of each sample, a 100-nm-thick serpentine Pt heater was patterned to define the 10 × 10 mm^2 heating area, which also served as a resistance temperature sensor for temperature characterization. For all tests, the boiling system was at atmospheric pressure with degassed high-purity de-ionized water. All samples were cleaned by argon plasma before boiling to

remove hydrocarbon contaminants.[38] To account for the lateral-conduction loss through the sample thickness, experimentally measured data were numerically calibrated (COMSOL Multiphysics 5.3a). The details of the experimental setup and boiling heat transfer characterization are given in Sections II and III of Supporting Information.

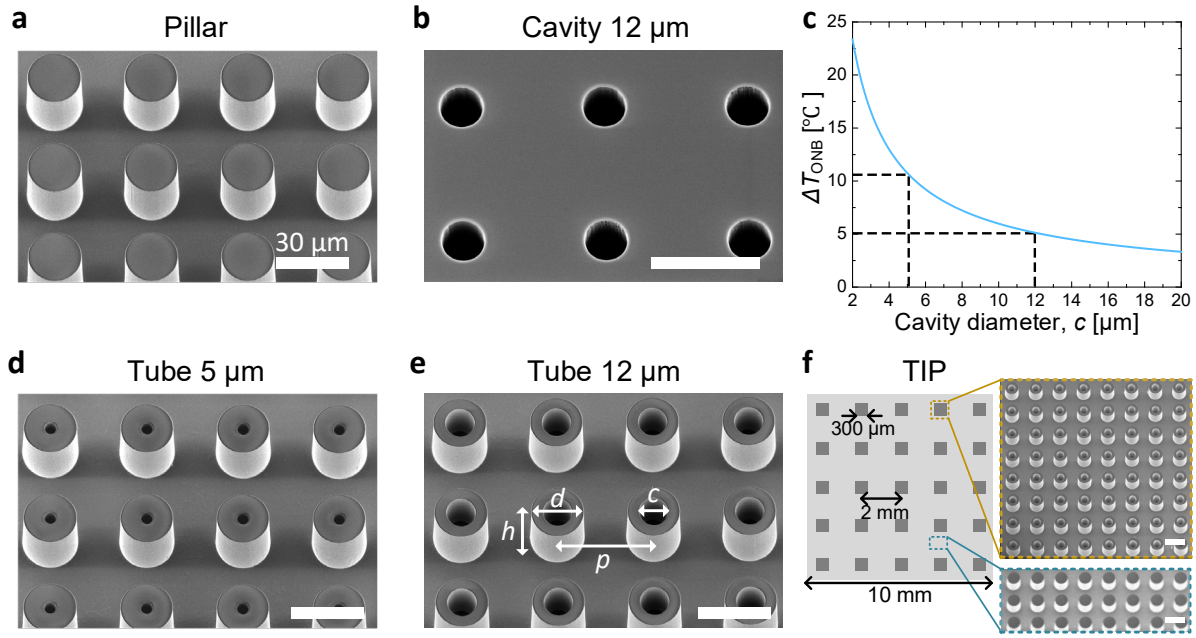

Figure 2. SEM images of fabricated microsurfaces and the onset of nucleate boiling temperature relationship with cavity diameter. (a) Micropillar arrays. (b) Microcavity arrays with 12-μm diameter. (c) Onset of nucleate boiling temperature as a function of cavity diameter. Cavities of 5 μm and 12 μm are fabricated to investigate the cavity size effects. (d) Microtube arrays with the cavity diameter of 5 μm. (e) Microtube arrays with the cavity diameter of 12 μm. (f) Schematics of boiling area of TIP (tube-clusters in pillars) surfaces where microtube clusters (300 × 300 μm^2, SEM image shown in an orange box) are separated from each other by cluster-to-cluster pitch of 2 mm with micropillars (SEM image shown in an aqua box) between the clusters. All SEM images are taken with 20° tilt angle and all scale bars are 30 μm.

RESULTS

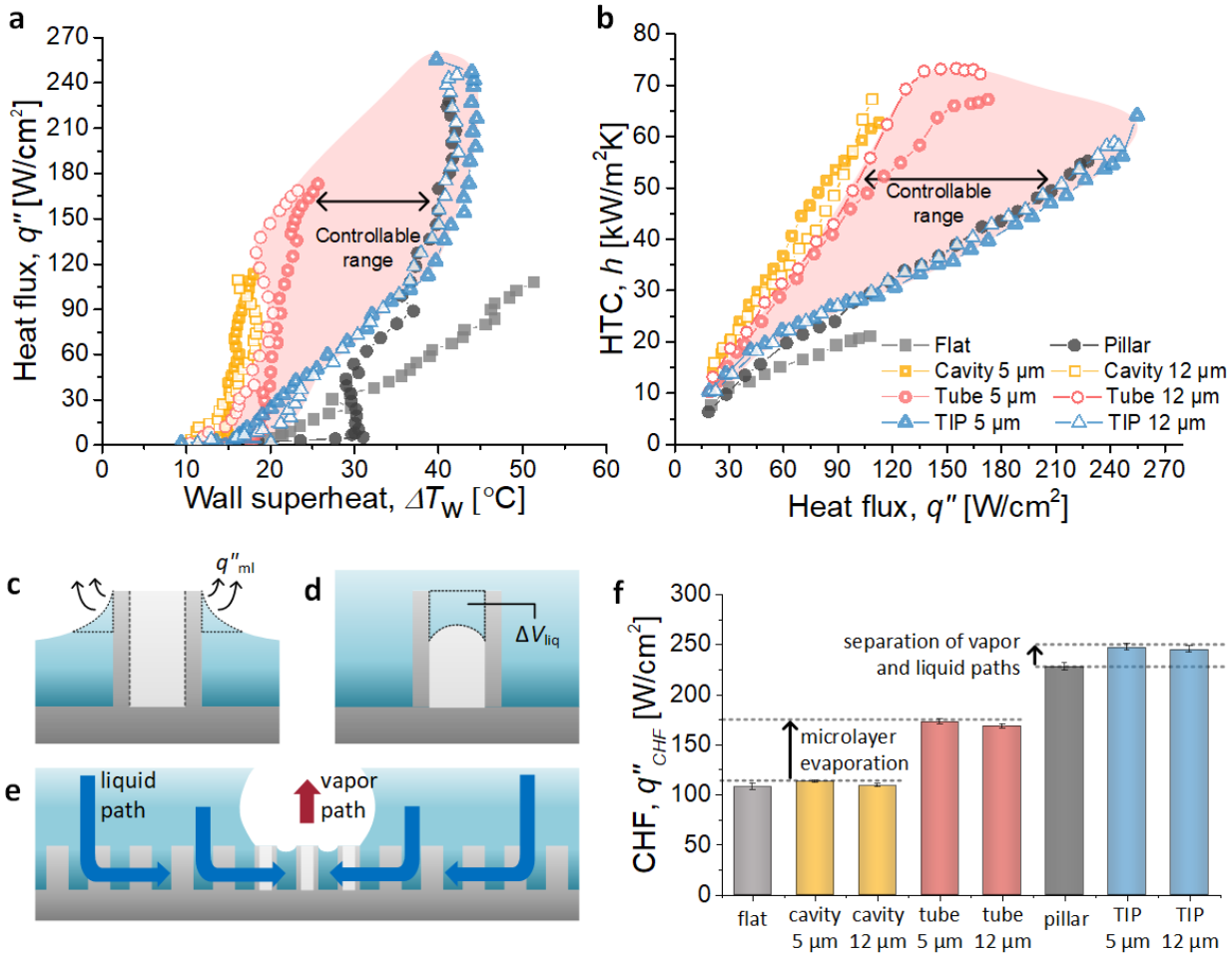

Figure 3. Pool boiling results and enhancement mechanisms of microtube and TIP surfaces. (a) Pool boiling curves of water on different surface structures. (b) Heat transfer coefficients as a function of boiling heat flux. For (a) and (b), the experimental uncertainty is smaller than the marker size. Shaded red areas show the range of boiling curves that can be obtained by controlling the cluster-to-cluster pitch of a TIP surface. Experimental uncertainty analysis is available in Supporting Information. (c – d) Schematics of cross-section view of a microtube during boiling. (c) Evaporative heat flux from the microlayer around the sidewalls of microtubes (q''_{ml}), which provides additional heat flux to microtube arrays compared to microcavity arrays. (d) Penetrated liquid with volume of ΔV_{liq} in a microtube cavity during the rewetting of liquid. Analytical estimation suggests that the evaporation of the penetrated liquid has minimal effects on CHF enhancement of TIP surfaces. (e) Schematic of the separated liquid and vapor paths on TIP surfaces. Bubbles are generated on top of microtube clusters, while rewetting liquids come from the outside of microtube clusters with minimal disturbance from growing bubbles. (f) CHF values for different surface structures and CHF enhancement mechanisms.

Figure 3a shows pool boiling curves with heat flux as a function of wall superheat for different surfaces. These curves were obtained by gradually increasing the heat flux up to the CHF point. By definition, CHF and HTC are the maximum heat flux and the slope of a point from the origin on a boiling curve, respectively. HTC is also plotted as a function of heat flux for a heat flux over 25 W/cm^2 in Figure 3b. In the plots, the structures with cavities, e.g., microcavity, microtube, and TIP surfaces, have open data symbols, where the open area of the data symbols represent the cavity size, i.e., the large and small open area represent the 12 μm and 5 μm cavity diameters, respectively. Compared to a flat surface (grey closed square), all structured surfaces showed enhancement of either or both HTC and CHF. As expected, we observed distinctly different effects of cavity and pillar structures on boiling behavior. The boiling curves of cavity arrays (orange open squares) showed significantly steeper slopes, i.e., higher HTC values, than that of flat and pillar surfaces (black closed circles), while their CHF values remained very close to the flat surface. Also, the larger cavity of 12 μm resulted in a higher HTC value than the smaller cavity of 5 μm near the onset of nucleate boiling, which was consistent with the theoretical prediction of the ΔT_{ONB}. Micropillar surfaces, on the other hand, showed significant enhancement of CHF, but no enhancement of HTC up to the wall superheat of ~30℃ due to the absence of artificial nucleation sites. The uniform microtube arrays (red open circles), which were designed to exploit the combined effects of cavity and pillar structures, enhanced HTC and CHF values simultaneously. Similar trends of HTC with uniform cavity arrays were observed, for example, the lower ΔT_{ONB} of tubes with 12 μm cavity than 5 μm. Compared to the flat surface, the HTC values of Tube 5 μm and Tube 12 μm at CHF points (h_{CHF}) were enhanced ~220% and ~244%, respectively. Moreover, Tube 5 μm and Tube 12 μm surfaces achieved 60% and 62% CHF enhancement, respectively, compared to the flat surface, presumably due to the

additional microlayer evaporation (q''_{ml}) around the sidewalls of microtubes (Figure 3c).[17, 39-40] The experimental results show that the CHF enhancement of microtube arrays was not as significant as that of micropillar arrays even though they both have the same surface wickability due to their identical sidewall geometries. The results indicate that the CHF values are not a function of single surface feature, i.e., surface wickability, but are a result of the collective behavior of stochastic bubble interactions, where nucleation site density, bubble departure frequency, and bubble diameter play important roles in addition to surface wickability. For microtube surfaces, the high nucleation site density and excessive coalescence of bubbles may lead to the earlier boiling crisis than that with micropillar surfaces.

Boiling curves of TIP surfaces (blue open hexagons) that separated microtube nucleation clusters from each other by 2 mm and included micropillar arrays between clusters corroborated our hypothesis. Both TIP surfaces showed slightly higher CHF values than that of uniform pillar arrays by minimizing bubble coalescence and fully exploiting the role of micropillars for CHF enhancement. Micropillar arrays, TIP 5 μm, and TIP 12 μm surfaces showed ~110%, ~138% and ~129% CHF enhancement, respectively. The additional CHF enhancement of TIP surfaces compared to micropillar arrays can be attributed to two factors: additional evaporation of penetrated liquid in the microtube cavities (Figure 3d) and effective separation of liquid and vapor paths, i.e., the bubble nucleation and departure regions are separated from the paths of the rewetting liquid (Figure 3e). The volume of penetrated liquid (ΔV_{liq}) during the rewetting of liquid and additional heat flux from its evaporation is, however, negligibly small (~0.06 W/cm^2) compared to the enhancement (27.2 W/cm^2 and 17.1 W/cm^2 for TIP 5 μm and TIP 12 μm, respectively) (See Supporting Information Section IV for detailed analysis). The additional CHF enhancement is therefore attributed to effective separation of liquid and vapor paths, where a

similar phenomenon has been observed in literature.[21] On TIP surfaces, bubbles are generated on top of microtube clusters; consequently, rewetting liquids may come from the top of micropillar arrays to under the bubbles with minimal disturbance. In contrast, uniform micropillar arrays have preferred nucleation sites at the bottom corners of pillars due to the local temperature concentration. Therefore, nucleating bubbles can block the paths of rewetting liquids during the bubble growth period, which would adversely affect CHF enhancement. We show CHF values of all surfaces in Figure 3f and their enhancement mechanisms.

It is also interesting to note that the boiling curves of TIP surfaces showed two different regimes due to two surface features (Figure 3a). In the early stage of nucleate boiling, $\Delta T_w < \sim 30°C$, promotion of nucleation from microtubes is dominant, which leads to a HTC enhancement compared to uniform pillar arrays. When $\Delta T_w > \sim 30°C$, the TIP boiling curves overlap with the boiling curve of the micropillars, which suggests that the evaporative heat transfer from the sidewalls of the micropillars is dominant. In addition, the results suggest that by controlling the cluster-to-cluster pitch, we can design TIP surfaces with a boiling curve located in between the uniform microtube arrays and the TIP surface with the cluster-to-cluster pitch of 2 mm (shaded red area). As the pitch becomes shorter and the density of microtube, i.e., nucleation sites, is higher, the effects of promoting bubble nucleation from microtubes become more dominant and the surface will enhance HTC more effectively than CHF; the opposite holds for the wider pitch and lower nucleation site density. This controllability may offer surface design flexibility to achieve a desired boiling curve according to the application.

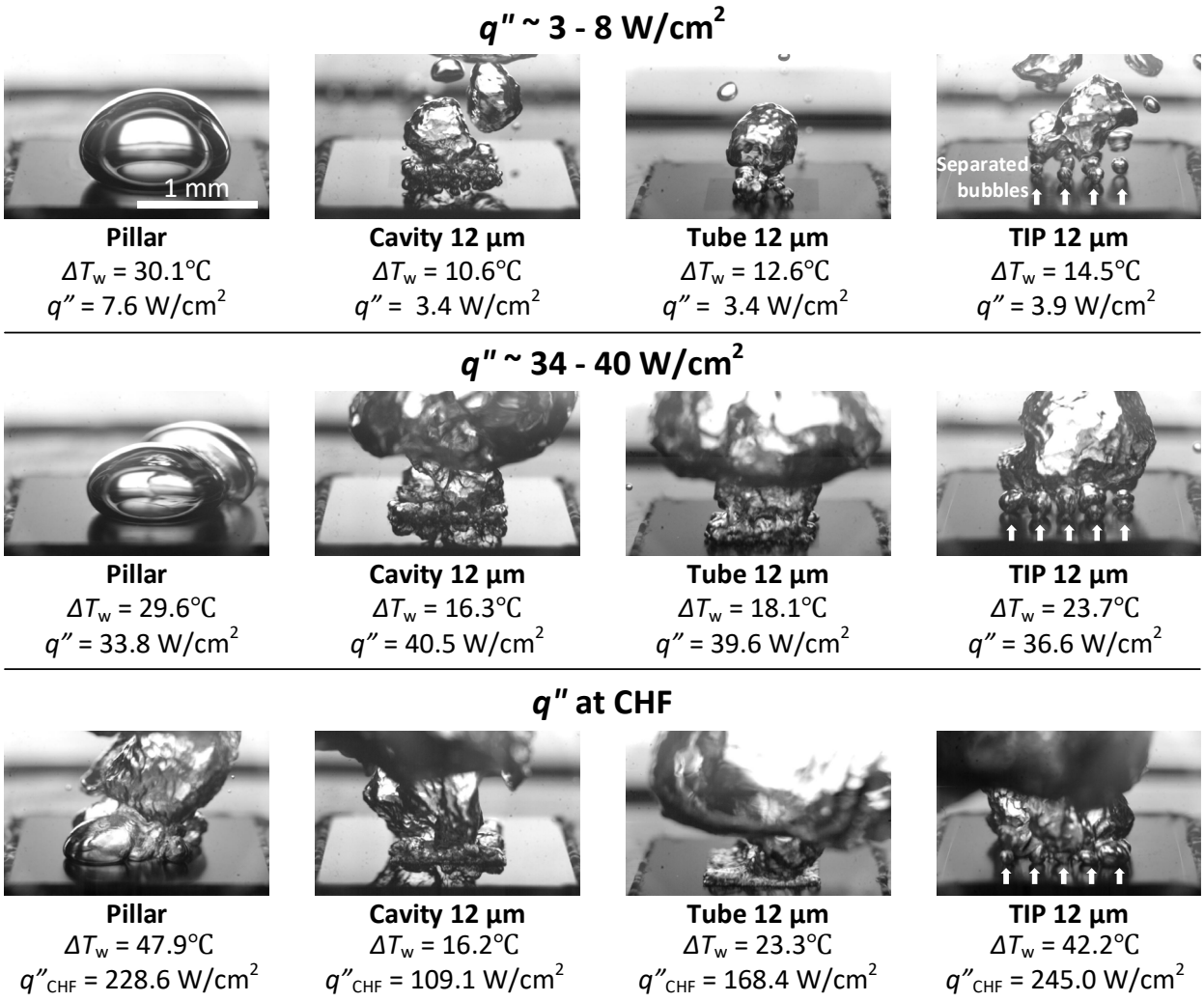

Figure 4. Images of boiling captured by a high-speed camera with up to 4000 frames per second. Each row shows the bubble dynamics at different heat flux ranges and each column represents different surface structures. The TIP 12 µm surface shows separated bubbles from microtube clusters, which are highlighted with white arrows. All images have the same scale and were taken with 19° tilt angle. High-speed movies of all surfaces including surfaces with 5 µm cavities are available in Supporting Information.

Imaging of the bubble dynamics (Figure 4) of different surface structures captured by a high-speed camera (Phantom v7.1, Vision Research) supports the boiling curve analysis (see Supporting Information for movies). Each row shows the bubble dynamics at different heat flux

ranges, e.g., ~ 3 – 8 W/cm^2, ~34 – 40 W/cm^2, and at CHF points, respectively, while each column represents different surface structures, e.g., Pillar, Cavity 12 μm. Tube 12 μm, and TIP 12 μm (from left to right). At the very early stage of nucleate boiling (q'' < 10 W/cm^2), the micropillar surface had noticeably different bubble dynamics compared to the other surfaces having artificial nucleation sites. Since the surfaces with cavities nucleated at very low superheat, there were small bubbles with high nucleation site density; in particular, TIP 12 μm showed separated bubbles nucleated from microtube clusters. The micropillar surface, on the contrary, had a large single bubble at this stage. The surface without artificial nucleation sites such as micropillar array generally required high wall superheat for nucleation, which led to the large bubble size since the inertia-driven bubble growth became more dominant.[41] Similar trends continued when the heat flux increased to ~34 – 40 W/cm^2 but the higher heat flux generated more active nucleation sites with higher bubble departure frequency. The bubble snapshots at CHF illustrated the CHF enhancement mechanisms on different surface structures. According to previous studies, the boiling crisis may be the result of stochastic interaction of bubbles, where active nucleation site density, bubble departure diameter, and departure frequency are important parameters for the interactions.[31-34] In the cases of Cavity 12 μm and Tube 12 μm, the coalesced bubbles formed vapor films over the boiling surfaces at CHF due to their extensively dense nucleation sites, which suggests that the high nucleation site density was the dominant triggering mechanism of the boiling crisis on these surfaces. The snapshots of micropillar arrays and TIP 12 μm showed, on the other hand, that boiling areas were not entirely covered by a vapor film; instead, parts of the boiling areas remained wet. This result suggests that, in addition to nucleation site density, other parameters such as bubble departure diameter and frequency also play important roles on determining CHF. In particular, TIP 12 μm showed that the majority of

bubbles were generated at microtube clusters even at CHF. Separated liquid and vapor paths facilitated rewetting of liquids in between the tube clusters and accelerated bubble departure from the clusters. This high-speed imaging analysis supports our findings from the boiling curve data that the additional CHF enhancement compared to uniform pillar arrays is attributed to effective separation of liquid and vapor paths of TIP surfaces.

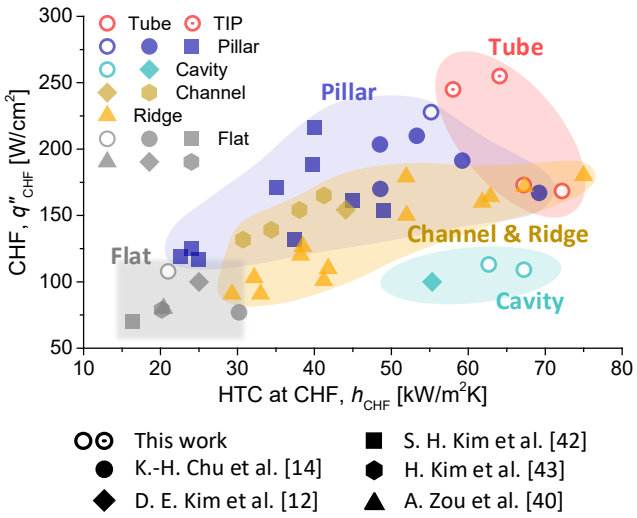

Figure 5. A regime map of CHF (q''_{CHF}) and HTC at CHF (h_{CHF}) values of different SiO_2 microstructured surfaces.

In Figure 5, we compared CHF (q''_{CHF}) and HTC at CHF (h_{CHF}) values of microtube structures with different microscale structures from literature data.[12, 14, 40, 42-43] Since surface wettability can also affect boiling performance, we included the data of SiO_2 surfaces to compare the sole effect of surface structure. We included the comparison of the data including nanostructures and other materials in Section VI of Supporting Information. Microcavity, channel, and ridge structures generally provide significant enhancement of HTC values, but CHF enhancement remains

limited to ~70%. On the contrary, micropillars can enhance CHF values more than 100%, but the enhancement of HTC values is not as high as in cavity, channel, and ridge structures. The proposed microtubes can provide significant simultaneous enhancement of CHF and HTC values and mark the top-right region of the plot in Figure 5. Combined with micropillars, the microtube structure may serve as a structural building block and provide design flexibility of boiling surfaces for enhanced pool boiling heat transfer.

CONCLUSIONS

In this work, we designed microtube structures for simultaneous enhancement of CHF and HTC values during pool boiling heat transfer. We analyzed pool boiling results and analyzed enhancement mechanisms with high-speed imaging. Uniform microtube arrays demonstrated simultaneous enhancement of CHF and HTC values up to 62% and 244%, respectively. The enhancement of HTC is attributed to active bubble nucleation from microtube cavities, while CHF enhancement is a result of microlayer evaporation around microtube sidewalls. Moreover, higher CHF values were achieved than that of uniform micropillar arrays with TIP surfaces by separating microtube clusters by 2 mm from each other within micro-pillars arrays. As a result, the earlier boiling crisis due to extensive bubble coalescence could be prevented. By changing the cluster-to-cluster pitch, our approach can be used to design TIP surfaces with boiling curves in between those of uniform micropillars and the TIP surface with the cluster-to-cluster pitch of 2 mm. In addition to promising boiling performance, this work provides guidelines for the systematic surface design of desired boiling parameters.

AUTHOR INFORMATION

Corresponding Author

*enwang@mit.edu

Author Contributions

Y. Song and E. N. Wang conceived the idea. Y. Song, S. Gong, and G. Vaartstra performed analytical modeling. Y. Song fabricated and tested microsurfaces. All authors contributed to the preparation of the manuscript.

ACKNOWLEDGMENT

The information, data, or work presented herein was funded in part by the Advanced Research Projects Agency-Energy (ARPA-E), U. S. Department of Energy, under Award Number DE-AR0000ABC. S. Gong would like to acknowledge the support from national Natural Science Foundation of China (No. 51706135), National Science and Technology Major Project (No. 2018ZX06002004), and Shanghai Pujiang Program (No. 20PJ1406800). G. Vaartstra would like to acknowledge support from the Air Force Office of Scientific Research under Grant No. FA9550-19-1-0392.

Supporting Information

Details of surface fabrication method, pool boiling experimental setup, numerical calibration of effective heat flux, analysis of penetrated liquid in microtube cavities, uncertainty analysis,

comparison of CHF and HTC values from literature data including other materials and nanostructures, high-speed movies of bubble dynamics on microstructured surfaces.

REFERENCES

1. Cho, H. J.; Preston, D. J.; Zhu, Y.; Wang, E. N. Nanoengineered Materials for Liquid–Vapour Phase-Change Heat Transfer. *Nat. Rev. Mater.* **2016**, *2*, 16092.
2. *Annual Energy Outlook 2020*; Washington, DC, **2020**; pp 1-162.
3. Mattila-Sandholm, T.; Wirtanen, G. Biofilm Formation in the Industry: A Review. *Food Rev. Int.* **1992**, *8*, 573-603.
4. Haryanto, A.; Fernando, S.; Murali, N.; Adhikari, S. Current Status of Hydrogen Production Techniques by Steam Reforming of Ethanol: A Review. *Energy & Fuels* **2005**, *19*, 2098-2106.
5. Humplik, T.; Lee, J.; O'Hern, S. C.; Fellman, B. A.; Baig, M. A.; Hassan, S. F.; Atieh, M. A.; Rahman, F.; Laoui, T.; Karnik, R.; Wang, E. N. Nanostructured Materials for Water Desalination. *Nanotechnology* **2011**, *22*, 292001.
6. Hansen, J. D.; Johnson, J. A.; Winter, D. A. History and Use of Heat in Pest Control: A Review. *Int. J. Pest Manage.* **2011**, *57*, 267-289.
7. Royne, A.; Dey, C. J.; Mills, D. R. Cooling of Photovoltaic Cells under Concentrated Illumination: A Critical Review. *Sol. Energy Mater. Sol. Cells* **2005**, *86*, 451-483.
8. Vasiliev, L. L. Heat Pipes in Modern Heat Exchangers. *Appl. Therm. Eng.* **2005**, *25*, 1-19.
9. Nukiyama, S. The Maximum and Minimum Values of the Heat Q Transmitted from Metal to Boiling Water under Atmospheric Pressure. *J. Jpn. Soc. Mech. Eng.* **1934**, *37*, 367-374.
10. Liu, Y.; Tang, J.; Li, L.; Shek, Y. N.; Xu, D. Design of Cassie-Wetting Nucleation Sites in Pool Boiling. *Int. J. Heat Mass Transfer* **2019**, *132*, 25-33.
11. Betz, A. R.; Jenkins, J.; Kim, C.-J. C.; Attinger, D. Boiling Heat Transfer on Superhydrophilic, Superhydrophobic, and Superbiphilic Surfaces. *Int. J. Heat Mass Transfer* **2013**, *57*, 733-741.
12. Kim, D. E.; Park, S. C.; Yu, D. I.; Kim, M. H.; Ahn, H. S. Enhanced Critical Heat Flux by Capillary Driven Liquid Flow on the Well-Designed Surface. *Appl. Phys. Lett.* **2015**, *107*, 023903.
13. Yu, C. K.; Lu, D. C.; Cheng, T. C. Pool Boiling Heat Transfer on Artificial Micro-Cavity Surfaces in Dielectric Fluid Fc-72. *J. Micromech. Microeng.* **2006**, *16*, 2092-2099.
14. Chu, K.-H.; Enright, R.; Wang, E. N. Structured Surfaces for Enhanced Pool Boiling Heat Transfer. *Appl. Phys. Lett.* **2012**, *100*, 241603.
15. Ahn, H. S.; Jo, H. J.; Kang, S. H.; Kim, M. H. Effect of Liquid Spreading Due to Nano/Microstructures on the Critical Heat Flux During Pool Boiling. *Appl. Phys. Lett.* **2011**, *98*, 071908.
16. Rahman, M. M.; Ölçeroğlu, E.; McCarthy, M. Role of Wickability on the Critical Heat Flux of Structured Superhydrophilic Surfaces. *Langmuir* **2014**, *30*, 11225-11234.
17. Dhillon, N. S.; Buongiorno, J.; Varanasi, K. K. Critical Heat Flux Maxima During Boiling Crisis on Textured Surfaces. *Nat. Commun.* **2015**, *6*, 8247.

18. Pham, Q. N.; Zhang, S.; Hao, S.; Montazeri, K.; Lin, C.-H.; Lee, J.; Mohraz, A.; Won, Y. Boiling Heat Transfer with a Well-Ordered Microporous Architecture. *ACS Appl. Mater. Interfaces* **2020**, *12*, 19174-19183.
19. Shim, D. I.; Choi, G.; Lee, N.; Kim, T.; Kim, B. S.; Cho, H. H. Enhancement of Pool Boiling Heat Transfer Using Aligned Silicon Nanowire Arrays. *ACS Appl. Mater. Interfaces* **2017**, *9*, 17595-17602.
20. Ahn, H. S.; Park, G.; Kim, J. M.; Kim, J.; Kim, M. H. The Effect of Water Absorption on Critical Heat Flux Enhancement During Pool Boiling. *Exp. Therm Fluid Sci.* **2012**, *42*, 187-195.
21. Jo, H.; Yu, D. I.; Noh, H.; Park, H. S.; Kim, M. H. Boiling on Spatially Controlled Heterogeneous Surfaces: Wettability Patterns on Microstructures. *Appl. Phys. Lett.* **2015**, *106*, 181602.
22. Choi, G.; Shim, D. I.; Lee, D.; Kim, B. S.; Cho, H. H. Enhanced Nucleate Boiling Using a Reduced Graphene Oxide-Coated Micropillar. *Int. Commun. Heat Mass Transfer* **2019**, *109*, 104331.
23. Patil, C. M.; Kandlikar, S. G. Pool Boiling Enhancement through Microporous Coatings Selectively Electrodeposited on Fin Tops of Open Microchannels. *Int. J. Heat Mass Transfer* **2014**, *79*, 816-828.
24. Jaikumar, A.; Kandlikar, S. G. Enhanced Pool Boiling Heat Transfer Mechanisms for Selectively Sintered Open Microchannels. *Int. J. Heat Mass Transfer* **2015**, *88*, 652-661.
25. Chu, K.-H.; Soo Joung, Y.; Enright, R.; Buie, C. R.; Wang, E. N. Hierarchically Structured Surfaces for Boiling Critical Heat Flux Enhancement. *Appl. Phys. Lett.* **2013**, *102*, 151602.
26. Može, M.; Senegačnik, M.; Gregorčič, P.; Hočevar, M.; Zupančič, M.; Golobič, I. Laser-Engineered Microcavity Surfaces with a Nanoscale Superhydrophobic Coating for Extreme Boiling Performance. *ACS Appl. Mater. Interfaces* **2020**, *12*, 24419-24431.
27. Wang, D.; Sun, Q.; Hokkanen, M. J.; Zhang, C.; Lin, F.-Y.; Liu, Q.; Zhu, S.-P.; Zhou, T.; Chang, Q.; He, B.; Zhou, Q.; Chen, L.; Wang, Z.; Ras, R. H. A.; Deng, X. Design of Robust Superhydrophobic Surfaces. *Nature* **2020**, *582*, 55-59.
28. Wilke, K. L.; Antao, D. S.; Cruz, S.; Iwata, R.; Zhao, Y.; Leroy, A.; Preston, D. J.; Wang, E. N. Polymer Infused Porous Surfaces for Robust, Thermally Conductive, Self-Healing Coatings for Dropwise Condensation. *ACS Nano* **2020**, *14*, 14878-14886.
29. Liter, S. G.; Kaviany, M. Pool-Boiling CHF Enhancement by Modulated Porous-Layer Coating: Theory and Experiment. *Int. J. Heat Mass Transfer* **2001**, *44*, 4287-4311.
30. Kandlikar, S. G. Controlling Bubble Motion over Heated Surface through Evaporation Momentum Force to Enhance Pool Boiling Heat Transfer. *Appl. Phys. Lett.* **2013**, *102*, 051611.
31. Lloveras, P.; Salvat-Pujol, F.; Truskinovsky, L.; Vives, E. Boiling Crisis as a Critical Phenomenon. *Phys. Rev. Lett.* **2012**, *108*, 215701.
32. Charignon, T.; Lloveras, P.; Chatain, D.; Truskinovsky, L.; Vives, E.; Beysens, D.; Nikolayev, V. S. Criticality in the Slowed-Down Boiling Crisis at Zero Gravity. *Phys. Rev. E* **2015**, *91*, 053007.
33. Zhang, L.; Seong, J. H.; Bucci, M. Percolative Scale-Free Behavior in the Boiling Crisis. *Phys. Rev. Lett.* **2019**, *122*, 134501.
34. Gong, S.; Zhang, L.; Cheng, P.; Wang, E. N. Understanding Triggering Mechanisms for Critical Heat Flux in Pool Boiling Based on Direct Numerical Simulations. *Int. J. Heat Mass Transfer* **2020**, *163*, 120546.

35. Griffith, P.; Wallis, J. D. The Role of Surface Conditions in Nucleate Boiling. *Chemical Engineering Progress Symposium Series* **1958**, *56*, 49-63.
36. Hsu, Y. Y. On the Size Range of Active Nucleation Cavities on a Heating Surface. *J. Heat Transfer* **1962**, *84*, 207-213.
37. Jaikumar, A.; Emery, T. S.; Kandlikar, S. G. Interplay between Developing Flow Length and Bubble Departure Diameter During Macroconvection Enhanced Pool Boiling. *Appl. Phys. Lett.* **2018**, *112*, 071603.
38. Song, Y.; Zhang, L.; Liu, Z.; Preston, D. J.; Wang, E. N. Effects of Airborne Hydrocarbon Adsorption on Pool Boiling Heat Transfer. *Appl. Phys. Lett.* **2020**, *116*, 253702.
39. Adera, S.; Antao, D.; Raj, R.; Wang, E. N. Design of Micropillar Wicks for Thin-Film Evaporation. *Int. J. Heat Mass Transfer* **2016**, *101*, 280-294.
40. Zou, A.; Singh, D. P.; Maroo, S. C. Early Evaporation of Microlayer for Boiling Heat Transfer Enhancement. *Langmuir* **2016**, *32*, 10808-10814.
41. Mikic, B. B.; Rohsenow, W. M.; Griffith, P. On Bubble Growth Rates. *Int. J. Heat Mass Transfer* **1970**, *13*, 657-666.
42. Kim, S. H.; Lee, G. C.; Kang, J. Y.; Moriyama, K.; Kim, M. H.; Park, H. S. Boiling Heat Transfer and Critical Heat Flux Evaluation of the Pool Boiling on Micro Structured Surface. *Int. J. Heat Mass Transfer* **2015**, *91*, 1140-1147.
43. Kim, H.; Ahn, H. S.; Kwak, H. J.; Kim, M. H.; Kim, D. E. Boiling Crisis Controlled by Capillary Pumping and Viscous Friction: Liquid Penetration Length and Dry Spot Diameter. *Appl. Phys. Lett.* **2016**, *109*, 243901.

Table of Contents (ToC)